Mapping of air quality products from VIIRS and TROPOMI

Additional Master Thesis

TU Delft // KNMI

Juliëtte Anema
June 30, 2019

Supervisors:
Dr. T. Vlemmix, KNMI
Dr. S. Basu, TU Delft
Dr. P. Veefkind, TU Delft & KNMI

Contents

Glossary

AMF Air Mass Factor

AOT Aerosol Optical Thickness

APSP Aerosol Particle Size Parameter (Ångström Exponent)

CALIOP Cloud-Aerosol Lidar with Orthogonal Polarisation

CLASS Comprehensive Large Array-data Stewardship System

DNB Day Night Band

DOAS Differential Optical Absorption Spectroscopy

EDR Environmental Data Records

ENVISAT Environmental Satellite

ERS-2 European Remote-Sensing Satellite 2

FIRMS Fire Information for Resource Management System

GOME Global Ozone Monitoring Experiment

GUI Graphic User Interface

I-Band Imagery Band

IP Intermediate Product

KNMI Koninklijk Nederlands Meteorologisch Instituut

LUT Look-up table

M-Band Moderate Band

MODIS Moderate Resolution Imaging Spectroradiometer

NASA National Aeronautics and Space Administration

NIR Near Infrared

NOAA National Oceanic and Atmospheric Administration

NRT Near Real Time

OEM Optimal Estimation Method

OMI Ozone Monitoring Instrument

QF Quality Flag

RDR Raw Data Records

RTM Radiative Transfer Model

S5-P Sentinel-5 Precursor

SCD Slanted Column Density

SCIAMACHY SCanning Imaging Absorption SpectroMeter for Atmospheric CHartographY

SDR Sensor Data Records

SUOMI-NPP Suomi National Polar-orbiting Partnership

SWIR Short Wavelength Infrared

TOA Top of Atmosphere

TROPOMI TROPOspheric Monitoring Instrument

UV Ultraviolet

VCD Vertical Column Density

VCM VIIRS cloud mask

VIIRS Visible/Infrared Imager/Radiometer Suite

VIS Visible

WHO World Health Organization

1. Introduction

Satellite remote sensing of air quality provides data regarding the quantities and distribution of atmospheric air pollutants on a global scale. The importance of knowledge concerning common air pollutants, such as trace gases and aerosols, comes from their influence on health and impacts on the Earth's heat balance (Figure 1.1). Nowadays air pollution forms the biggest environmental risk to health and is even stated to be a public health emergency (World Health Organization, 2016). According to the World Health Organization (WHO), monitoring of the air quality is the first step that will be needed to take by the public authorities.

The relation between and advantages of integrated use of ground and space-based measurements for air quality studies is broadly examined, e.g. (Gupta et al., 2006; Balis et al., 2007; Engel-Cox et al., 2004). Space-born observations are capable of providing repetitive measurements covering large, up to global, coverage. Especially the transportation and examination of the source of pollutants are growing applications in the field since satellite observations (Gupta et al., 2006).

Space based remote sensing of the atmosphere concerns the exploitation of the changing electromagnetic radiation by interactions with trace constituents and reflection by Earth's surface (Burrows et al., 2011; Martin, 2008). In active remote sensing, the satellite is the emitter and receiver of the radiation. In passive remote sensing, the initial radiation comes from the Sun (UV-vis, NIR, SWIR spectrum) and radiation emitted from Earth itself (thermal infrared). For air quality and climate monitoring, passive remote sensing instruments are especially interesting due to their broad tracks (Sanders et al., 2012). Wide swath width enable the satellite to cover the Earth in fewer orbits. Due to scattering, elastic and inelastic, and absorption processes some radiation will be lost, depending on wavelength and trace constituents, when traveling through the not-completely transparant atmosphere (Figure 1.2). For elastic scattering, Rayleigh and Mie scattering, the energy and wavelengths of the scattered photons do not change. While, for the inelastic Raman scattering the energy and wavelengths do not remain constant.

The analysis of atmospheric absorptions is the primary method for the identification of trace gases. Unique spectral fingerprints of the trace gases are recognizable in the reflectance spectrum. This enables the recognition of the gases in the spectra (Figure 2.5).The reflectance spectrum is the measured radiance spectrum divided by the highly structured solar spectrum. Subtraction of the highly structured solar spectrum is needed in order to reveal the spectral influences of the specific trace gases.

The monitoring of the distributions and amounts of trace constituents in the troposphere with the use of satellites began in 1995 with the launch of the GOME on-board ERS-2 (Burrows et al., 1999). In 2002, although much earlier developed in 1984-1988, SCIAMACHY on-board ENVISAT followed (Bovensmann et al., 1999). Both GOME and SCIAMCHY relied on spectrometers for their measurements of backscattered solar radiation in nadir (looking downwards). OMI contributed in 2004 on-board Aura with a spatial resolution of 13×24 km^2 (Levelt and Noordhoek, 2002). GOME, SCIAMCHY and OMI were optimized for the observations of trace gases. Alongside OMI aerosol space-borne sensors CALIOP, active lidar instrument, and MODIS, passive spectro-radiometer instrument, fly in NASA's A-train Satellite Constellation. In order to keep providing continuous time-series of important climate-forming factors NASA launched the Visible Infrared Imaging Radiometer Suite (VIIRS) instrument aboard Suomi NPP in 2011 (Murphy et al., 2001).

Like its predecessor MODIS, VIIRS also flies in close formation with a space-borne sen-

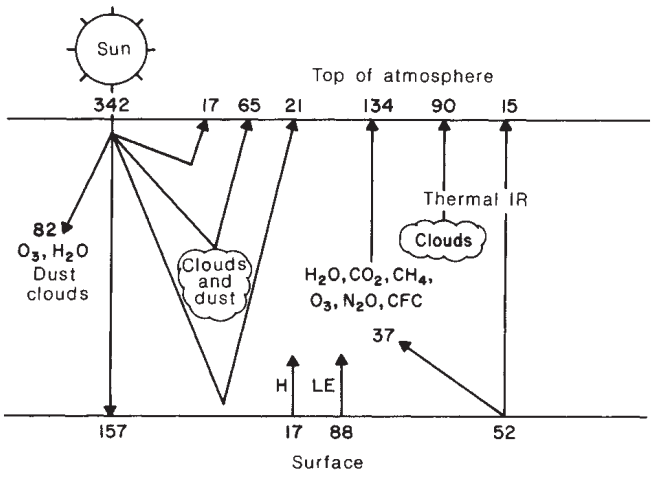

Figure 1.1: Schematic presenting the average fluxes (in W/m^2) of radiation of the Earth's climate system. Incoming solar radiation is affected by absorption and reflection. Some of the absorbed solar radiation returns back to space as thermal infrared radiation. An increase in the concentration of greenhouse trace gases reduce the thermal flux to space and therefore have a warming effect. Figure retrieved from (Dickinson and Cicerone, 1986).

sor optimized for trace gas detection, namely with the TROPOspheric Monitoring Instrument (TROPOMI). TROPOMI is the most recent contribution to the UV-VIS-NIR-SWIR passive hyper spectral instrument series launched on 13 October 2017 on board Sentinel-5 Precursor. The sensor measures a variety of trace gases (e.g. O_3, NO_2, SO_2, CO, CH_4) from backscattered solar radiation measurements in nadir. Sentinel-5P's swath remains within the scene observed by the Suomi-NPP. The strength of satellites being in close formation lays in the synergies among the sensors aboard. Combination of several products could lead to potential research products. The main objective for the selection of the Sentinel-5P's orbit to be in close formation with the NASA satellite came from the high spatial resolution observation capabilities of VIIRS (Siddans and Smith, 2018; Sanders et al., 2012) (due to use of thermal infrared). Figure 1.4 illustrates the position and properties of the different wavelength bands of VIIRS and TROPOMI. Like the A-train, S5-P and Suomi-NPP cross the equator in an ascending node in the early afternoon, around 13:30. During this time the atmospheric boundary layer is fully developed. Furthermore, measurements during the afternoon give a good representation of the trace gases coming from an anthropogenic emission source, since most activities take place during the day (Veefkind et al., 2012). The same equator crossing time of OMI and TROPOMI is valuable in detecting trends in a long continuous data record of both instruments. Furthermore, the very stable OMI (Levelt et al., 2018) instrument helps in the validation process of TROPOMI.

This report will focus on the use of both TROPOMI trace gas tropospheric products and the VIIRS aerosol product, in particular Aerosol Optical Thickness (AOT). The products will be used to provide maps showing the combined VIIRS and TROPOMI information. The narrow temporal separation between the instruments, less than 5 minutes (Siddans and Smith, 2018), makes it interesting to use VIIRS and TROPOMI, respectively, for aerosol and trace gas observations in combination for air quality monitoring.

Case studies

The air quality products from VIIRS and TROPOMI will be mapped for two different case studies:

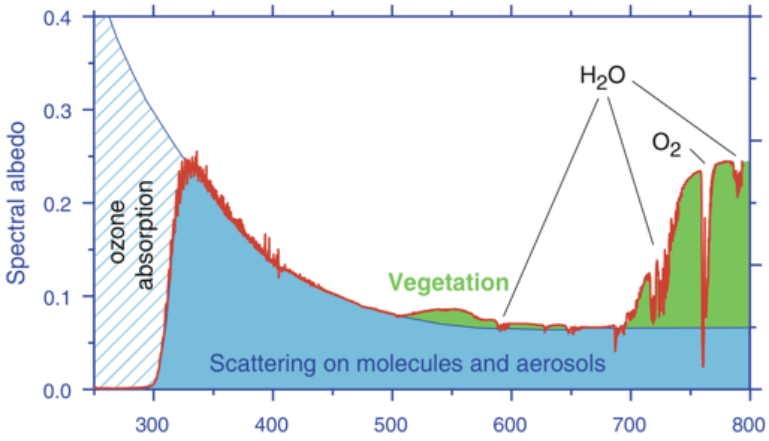

Figure 1.2: Reflectance spectra as a function of wavelength presenting the scattering effects on air molecules and aerosols as well as features of strong atmospheric absorbers (e.g. O_3, H_2O and O_2). Weak atmospheric absorbers could be analyzed by application of, e.g., the DOAS method (discussed in chapter 2.2.1). Figure retrieved from (Burrows et al., 2011).

- Air pollution in the Netherlands as a result of traditional Easter fires
  Traditional Easter fires cause a yearly returning pollution peak of several trace constituents in the atmosphere. Although being controlled and being short term, biomass burning can have negative influence on the air quality. Graveland et al. (2011) found a correlation between increased markers of airway inflammation and a high concentration of particulate matter associated with Easter fires. With the help of remote sensing biomass burning, such as the Easter fires can be tracked. The dates that will be plotted are 19-05-'19 till 22-05-'19.

- Air pollution in New Delhi
  The city of New Delhi experienced rapid growth in the last 50 years. This growth was accompanied by enhanced anthropogenic activities, e.g. fossil fuel combustion, biomass burning and increase in power production. The ambient air quality conditions vary over time due to several factors, e.g. weather related factors, influencing the air pollution on New Delhi (Gopalaswami, 2016). The AOT and trace gas concentration data between 30-05-2019 and 02-06-2019 of the New Delhi region will be mapped. The true color composite images (figure 4.7) show an increase of the air pollution, recognizable as the white haze, over this period.

Objectives

The objective of this project is to provide accessible python-based tools that enable downloading and visualization of both VIIRS EDR AOT and TROPOMI trace gas data for the purpose of air quality analysis.

Overview

Chapter 2 contains a literature review on the AOT VIIRS level 2 product (chapter 2.1) and Trace Gas TROPOMI level 2 products (chapter 2.2) in order to give insight into the retrieval methods of the products. Chapter 3 covers the methodology. The results, in chapter 4, will be used to demonstrate the possibilities of the developed scripts and Quality Flag GUI. We will look at trace gas concentration and AOT maps of the two case studies.

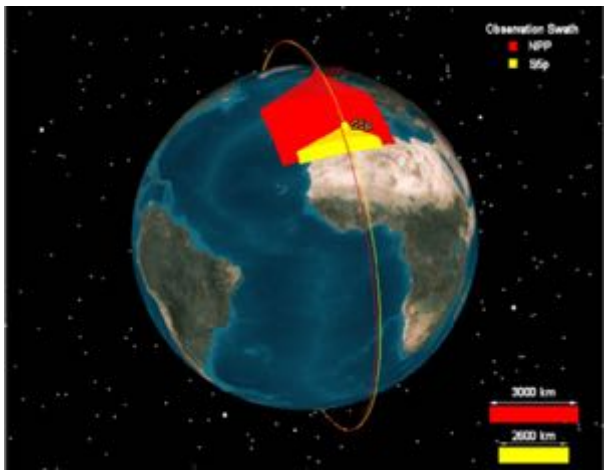

Figure 1.3: Illustration of the overlapping observation swaths of Sentinel-5P and Suomi-NPP. Both satellites have an equator crossing time near 13:30 local solar time. Retrieved from (ESA, 2019).

TROPOMI

	Band 1	Band 2	Band 3	Band 4	Band 5	Band 6	Band 7
Spectral range [nm]	270-300	300-320	310-405	405-500	675-725	725-775	2305-2385
Spectral resolution [nm]	1	0.5	0.55	0.55	0.5	0.5	0.25
Spectral sampling [nm]	0.065	0.065	0.2	0.2	0.1	0.1	<0.1
Spatial sampling [km^2]	21x28	7x7	7x7	7x7	7x7	7x7	7x7

VIIRS

	M12	M13	M14	M15	I5	M16
[1]	3660-3840	3973-4128	8400-8700	10263-11263	10500-12400	11538-12488
[2]	742x776	742x259	742x776	742x776	371x387	742x776
[3]	1.6x1.58	1.6x1.58	1.6x1.58	1.6x1.58	0.8x0.79	1.6x1.58

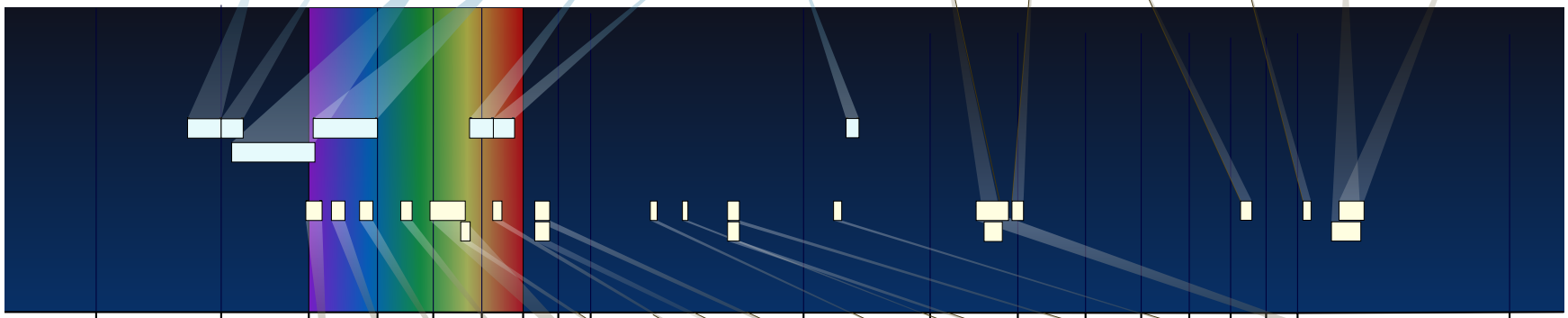

	M1	M2	M3	M4	I1	M5	M6	I2	M7	M8	M9	I3	M10	M11	I4
[1] Spectral range [nm]	402-422	436-454	478-498	545-565	600-680	662-682	739-754	846-885	846-885	1230-1250	1371-1386	1580-1640	1580-1640	2225-2275	3550-3930
[2] Spatial sampling - nadir [m^2]	742x259	742x259	742x259	742x259	371x387	742x259	742x776	371x387	742x259	742x776	742x776	371x387	742x776	742x776	371x387
[3] Spatial sampling - end scan [km^2]	1.6x1.58	1.6x1.58	1.6x1.58	1.6x1.58	0.8x0.79	1.6x1.58	1.6x1.58	0.8x0.79	1.6x1.58	1.6x1.58	1.6x1.58	0.8x0.79	1.6x1.58	1.6x1.58	0.8x0.79

VIIRS

Figure 1.4: Comparison position and properties of wavelength bands VIIRS and TROPOMI.

2. Literature

2.1 Aerosol Optical Thickness (AOT) VIIRS product

VIIRS is a broadband radiometer instrument with 22 spectral bands ranging from 412 nm to 12050 nm (figure 1.4) and a swath width of 3040 km. The instrument contains 3 type of bands: 16 M-bands with ∼750 m resolution at nadir, 5 I-bands with ∼ 375 m resolution at nadir and one Day Night Band (DNB). Due to pixel aggregation techniques the pixel growth towards the side of the swath is limited to twice the nadir resolution. As a result the pixels at nadir and towards the end are comparable. This is an improvement in comparison with MODIS where the pixels grew with a factor of 4 towards the side (NOAA NESDIS STAR, 2013b; Jackson et al., 2013). After the pixel aggregation process a 'bow-tie removal' approach is completed in order to delete overlapping pixels between adjacent scans (Jackson et al., 2013; Seaman, 2013; NOAA NESDIS STAR, 2014).

The VIIRS data are divided into the Raw Data Records (RDR, level 0), Sensor Data Record (SDR, level 1) and Environmental Data Records (EDR, level 2). The on board generated RDR data are the input for the calibrated SDR output. The EDR data is computed by the aggregation of 8×8 IP retrievals, see the schematic in figure 2.1. The EDR and IP data have resolutions of, respectively, 6 and 0.75 km. The Intermediate Products (IPs), such as VIIRS cloud mask (VCM) and AOT, are retrieved byproducts used for primary product generation or for the purpose of secondary processing (NOAA NESDIS STAR, 2014).

The aerosol products are mainly retrieved from the M-band SDRs in the visible to short-wave infrared spectral regions (412-2250 nm). In order to limit measured gas absorption the bandwidths of the bands are narrow.

Quality Flags

Pixels that are flagged as bad during the verification proces of the RDR data are passed through to the SDR output quality flags. Furthermore, the quality at pixel level is determined by multiple VIIRS aerosol algorithm tests of unfavourable conditions. Based on these classification results, the pixels used for the creation of the EDR are selected. The AOT IP contains four quality flag conditions: Not produced, Excluded, Degraded and High (table 2.1). During the IP to EDR aggregation process, the EDR quality flags are set based on the IP QF's (see figure 2.1). EDR QF's consists of 5 groups (QF1-QF5), each QF contains multiple flag values in 8-bit integer format. The EDR Quality Flags are discussed in detail in appendix C.2. of NASA (2019).

2.1.1 AOT and the retrieval

VIIRS measures the reflected solar radiation in multiple channels in the VIS, NIR and SWIR regions. The algorithm iterates through the several aerosol microphysical models and increases the AOT value to find a modeled solution that matches the reflectance measurements (Jackson et al., 2013). Since clouds have a large effect on the top of atmosphere (TOA) radiance aerosol retrieval will only be applied on cloud-free pixels. Note that there is a difference in the retrieval of aerosol properties over land and over the ocean surfaces. The ocean surface reflectance is more homogeneous and therefore more easily modeled. Furthermore, the separation of the effects of the reflectance of the dark ocean surface and the scattering aerosols is less challenging. The plots in figure 2.2 represent the higher uncertainty in the AOT retrieval over land. The interfering signals of a more bright ocean surface due to the effects of a sun glint is limited by avoiding of the specific pixels. The sun glint information comes from the VCM or from calculation by a

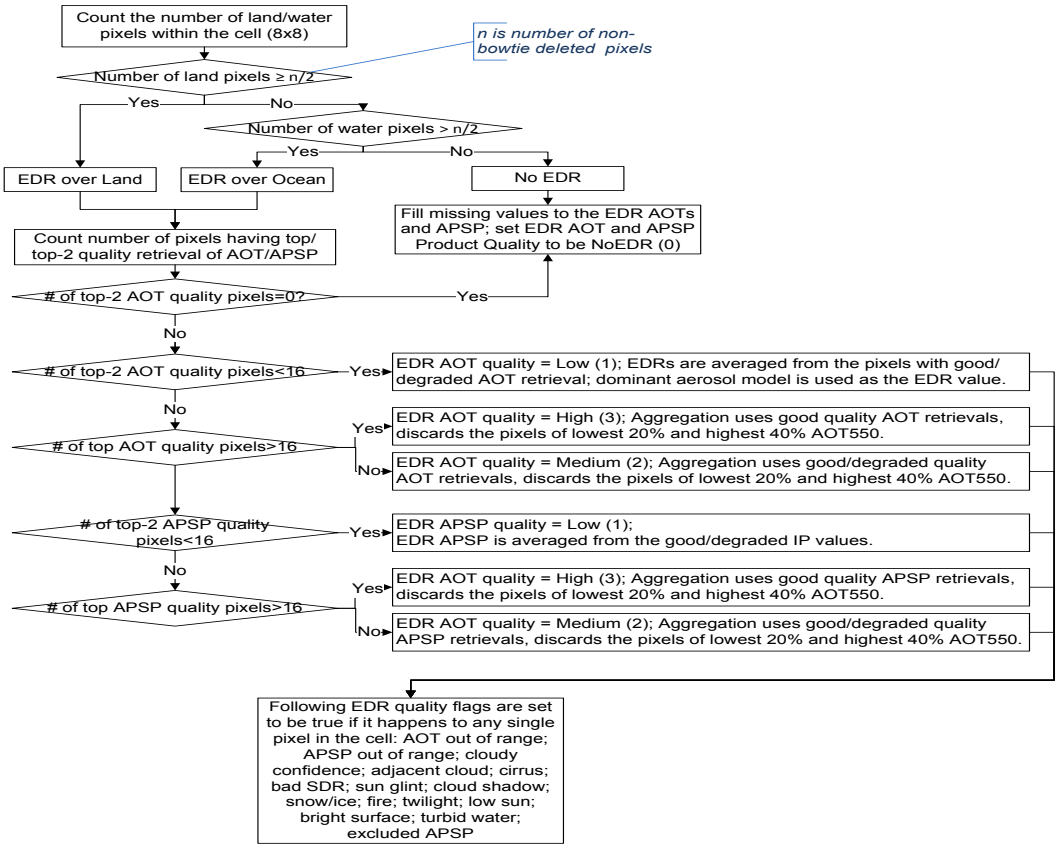

Figure 2.1: Schematic of IP to EDR integration from (NOAA NESDIS STAR, 2014). The 'top-2' quality flags at pixel level refer to 'Degraded' and 'High' (conditions described in 2.1)

	Not Produced	Excluded	Degraded	High
AOT	Solar zenith angle > 80º; Missing or saturated channel reflectance (L: M1, M2, M3, M5, M8, M11; O: M5, M6, M7, M8, M10, M11); Missing ancillary data (wind speed, wind direction, precipitable water, surface air temperature, column ozone, surface pressure); Probably or confidently cloudy; Snow/ice present; Fire present; Inland or coastal water; Sun glint present; Turbid water present; Bright surface present.	Retrieved AOT at 550nm is out of spec range (0.0-2.0); Missing channel reflectance/brightness temperature (L: M7, M9, M10, M12, M15, M16; O: M3, M4, M15, M16)	65º ≤ Solar Zenith Angle < 80º Cloud shadow present; Cirrus present; Adjacent pixel probably or confidently cloudy; Volcanic ash present; Soil dominant pixel; Retrieval residual beyond threshold.	Otherwise

Table 2.1: Pixel-level quality flag conditions for AOT. Retrieved from (NOAA NESDIS STAR, 2013a).

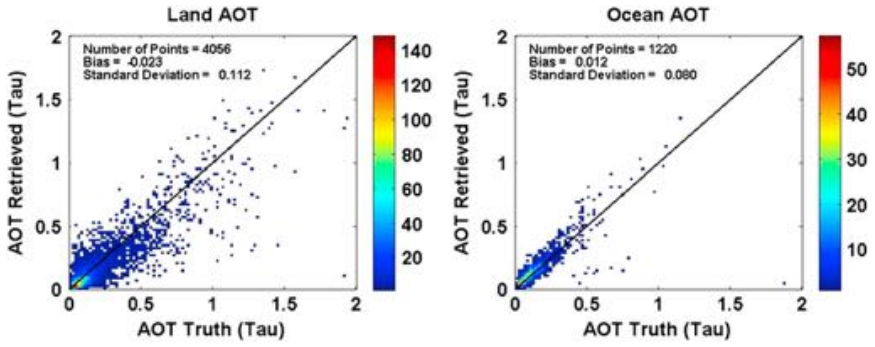

Figure 2.2: Retrieved VIIRS AOT at 550 nm EDR vs. AERONET level 1.5 measurements over land and ocean. Figure retrieved from: (Jackson et al., 2013). The plots show a higher standard deviation for the AOT data retrieved over land.

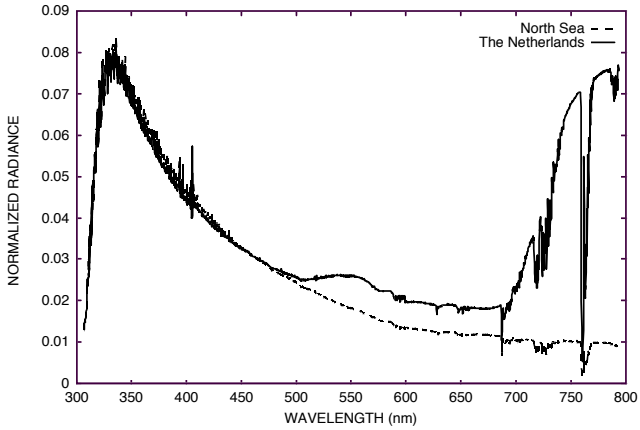

Figure 2.3: Normalized radiance, TOA radiance divided by extraterrestrial solar irradiance, as a function of wavelength. Measured by GOME. The normalized radiance over the North Sea and over the Netherlands differ little between wavelengths 340-400 nm (UV). The land albedo is low in this wavelength range. Figure retrieved from (Veefkind, 1999).

radiation transfer model (NASA, 2019). For the heterogeneous bright land surface, figure 2.3, the segregation of the aerosol interactions and the surface reflection of the incoming radiation is more difficult. (Veefkind, 1999; NASA, 2019)

2.2 Trace gases TROPOMI products

TROPOMI is a spectrometer instrument that measures in the ultraviolet and visible (UV/vis) (270-500 nm), near-infrared (NIR) (675-775 nm) and shortwave infrared (SWIR) (2305-2385 nm) (figure 1.4) spectral bands from a Sun-synchronous polar orbit with a swath width of 2600 km. These properties enable the instrument to obtain high accuracy daily global coverage measurements of, e.g., several important atmospheric trace gases with a high spatial resolution of up to 7×7 km^2. The tropospheric columns of O_3, NO_2, SO_2, BrO, HCHO and H_2O are measured from the UV-VIS-NIR wavelength range, whereas the tropospheric columns of CO and CH_4 are measured from the SWIR wavelength range. (Lambert et al., 2018; Voors et al., 2012)

The high spectral resolution of TROPOMI enables the sensor to distinguish more accurately

between the unique spectral signatures of different trace gases. Due to the high spatial resolution of TROPOMI, the instrument is able to detect small emissions plumes on a daily scale (Theys et al., 2019). A more frequent detection of weak plumes is of great value for the monitoring of point source pollutions.

2.2.1 Retrieval Concentration Trace gases

As described in the introduction (chapter 1), the processes affecting the propagation of radiation through the atmosphere are distinguished between absorption and different scattering processes. The algorithms used to retrieve the vertical columns make use of the spectral signatures of each individual trace gas. In this subsection the theory behind the retrieval algorithms will be briefly discussed. The retrieval of the Level-2 products based on the UV-VIS-NIR spectral ranges and of the SWIR spectral ranges will be treated separately.

Level-2 products based on UV-VIS-NIR

An appropriate spectral region will be needed to select for the retrieval of specific trace gases. Spectral regions with a high fluctuating absorption cross section, σ, are preferred as a result of their higher sensitivity. Each trace gas has its optimal wavelength interval for DOAS measurements (Platt and Stutz, 2008). The fitting window is selected such that it will limit the occurrence of interfering signals but maximizes the differential absorption structures of the trace gases of interest. Due to strong dependence of e.g Rayleigh scattering on wavelength, spectral retrieval and radiative transfer calculations are not identical for the retrieval of column densities at a large range of wavelength. This is the main reason for the use of small fitting windows. The analysis of the backscattered data in order to retrieve the vertical columns consists of two main steps. i) Analysis of the spectra. Based on the Differential Optical Absorption Spectroscopy (DOAS) or Optimal Estimation Method (OEM)the Slant Column Density (SCD/N^S) will be obtained. ii) Radiative Transfer Modeling (RTM) will be preformed for the conversion of the trace gas SCD to the gas concentration -or- Vertical Column Density (VCD/N^V)(see Figure 2.4). In order to convert the SCD to the VCD, the air mass factor (AMF) will be invoked. Since multiple parameters and processes influence the measured slant column, accurate computations of the air mass factor are needed for reliable retrievals of the trace gas concentrations (Slusser et al., 1996). The conversion is especially complicated by the fact that the ensemble photons arriving at the detector all have different light paths.

In the case of little Rayleigh scattering, e.g. for nadir observations in NIR, the AMF can be determined with the help of simple geometry. This simple relation is also visible in Figure 2.4.

$$AMF = \frac{SCD}{VCD} \tag{2.1}$$

$$AMF = \frac{1}{\cos(\theta)} + \frac{1}{\cos(\theta_0)} \tag{2.2}$$

However, the calculation of AMF will be more complex for the cases where the effects of Rayleigh scattering are not negligible. Therefore, Numerical radiative transfer simulations will be necessary for most of the measurements. For the computation of the Air Mass Factor's, pre-calculated Look-Up Tables (LUTs) or direct RTM's can be used. For the LUTs, radiative transfer calculations are used, for a variety of situations, outside of the retrieval algorithm. The different situations include the dependency parameters of AMF. The Air Mass Factor depends on the average light path. Therefore it is reliant on several parameters such as; wavelength, surface albedo, surface pressure, cloud fraction, aerosols and the vertical distribution of the trace gas. Since the light path is mostly affected by scattering, the vertical column density of the trace gas itself is only a dominant term for optically thick absorbers (Burrows et al., 2011). Since the

AMF depends strongly on the vertical profile, the total AMF will be obtained by the integration of the altitude-resolved AMF over height.

$$AMF = \frac{\int n(z)m(z)}{\int n(z)dz} \tag{2.3}$$

The results of the calculations are stored in look-up tables as function of several parameters (Burrows et al., 2011). As a result of the smaller pixels of TROPOMI more reference points are needed, in comparison with the courser OMI, to respect the increase in variability of the used parameters (van Geffen et al., 2019).

i) The idea behind the application of DOAS is to isolate the narrow spectral structures of the absorption spectra of the trace gases in question. The technique of absorption spectroscopy uses the absorption of electromagnetic radiation by matter. The absorption is expressed by the Lambert-Beer law.

$$\begin{aligned} I(\lambda) &= I_0(\lambda) \cdot e^{-\sigma(\lambda)\cdot\int \rho(x)\,dx} \\ &= I_0(\lambda) \cdot e^{-\sigma(\lambda)\cdot SCD} = I_0(\lambda) \cdot e^{-\tau(\lambda)} \end{aligned} \tag{2.4}$$

The absorption cross section σ at wavelength λ is specific for species. The integral of the trace gas concentration of the absorber over the light path gives the SCD.

In order to obtain the fine scaled structure of the absorption signal, differential cross section $\sigma^*(\lambda)$, the low frequency compartment, usually expressed as a low-order polynomial, is separated from the high frequency part (Burrows et al., 2011). The differential cross sections of the known absorbers are matched to the differential optical thickness spectrum (τ^*) by determination of the best combination of the scaling, N^S (Burrows et al., 2011).

$$\tau^* = ln\left(\frac{I_0(\lambda)}{I(\lambda)}\right) - P(\lambda) = \sum_j \sigma_j^*(\lambda) \cdot N_j^S \tag{2.5}$$

$$SCD = \frac{1}{\sigma} ln\left(\frac{I_0}{I}\right) \tag{2.6}$$

Since the stratospheric concentrations are not negligible for most species, except e.g. HCHO, a correction for the stratospheric column density will be needed (Burrows et al., 2011). If the stratospheric column density is known, the tropospheric concentration can be estimated. Especially for trace gases with a much higher density in the stratosphere than troposphere, such as O_3, accurate measurements of the stratospheric column density are needed to limit resulting errors on the tropospheric amount.

Note that the Optimal Estimation Method (OEM) usually will be used for the retrieval of trace gases with deeper absorption lines.

ii) Radiative transfer models simulate the effective light paths. As discussed previously, scattering and absorption processes in the atmosphere affect the propagation of radiation.

Level-2 products based on SWIR

Retrievals of Level-2 products from observations of backscattered solar radiation in the SWIR spectral range are accompanied by the interference of scattering by aerosols and clouds. In order to limit the uncertainty, cloud contaminated pixels will be filtered with the help of a SWIR pre-processing module before the retrieval processes.

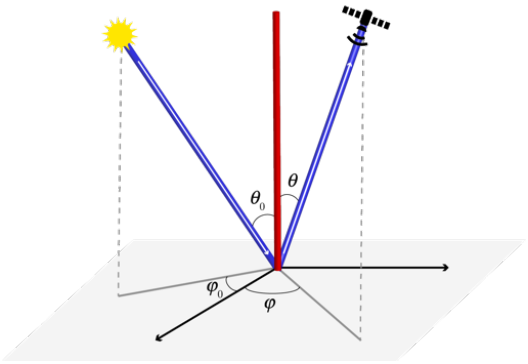

Figure 2.4: Illustration of the SCD (Slant Column Density) and the Vertical Column Density (VCD), presented as the red column. Solar azimuth angle (ϕ_0), Viewing azimuth angle (ϕ), Solar zenith angle (θ_0), Viewing zenith angle (θ)

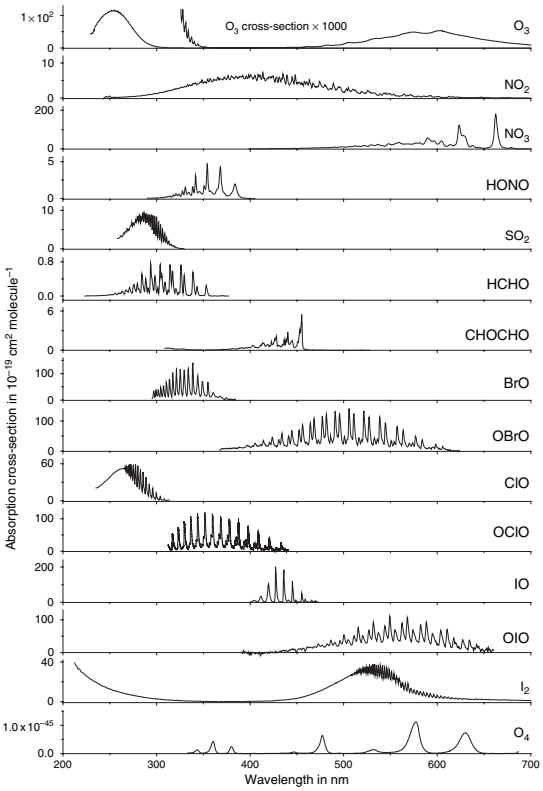

Figure 2.5: Unique patterns (Platt and Stutz, 2008)

3. Methods

Obtaining data, post-processing and mapping.

3.1 Selection dates case studies

The selection of days is based on the absence of clouds. For this selection true color images of NPP Suomi VIIRS from https://worldview.earthdata.nasa.gov were used. Clouds will appear white on the true color image.

3.2 Data

3.2.1 VIIRS EDR AOT data

The VIIRS data were obtained from the NOAA Comprehensive Large Array-data Stewardship System (CLASS) ftp server. The EDR product contains the AOT for 11 wavelengths. The AOT of 0.412 microns was used.

Post-processing

The post-processing and analyzing of the data has been done with the help of the developed python scripts. NOAA NESDIS STAR (2014) recommends the use of AOT QF's noted as high. Medium AOT quality could be used for some applications. Different degrees of masking were applied. For scenario 1 QF Cloud Contamination values were mapped. For scenario 2 QF Out of spec range values were mapped. Insight in the quality of the data was gained by the developed GUI. The obtained scripts and GUI are described into more depth in the user manual.

3.2.2 TROPOMI trace gases data

The TROPOMI trace gases data was downloaded using the download function of the python-based tool pyCAMA. pyCAMA interacts with the Copernicus data-hub for Sentinel-5P. The specific orbit numbers of the TROPOMI data were determined by subtracting the offset value from the orbit numbers of the selected VIIRS EDR data sets.

3.3 Mapping AOT and trace gas data

The AOT, NO_2, O_3, SO_2, HCHO, CO and CH_4 values for both scenario's were mapped. For scenario 1, the Netherlands, additional fire count data from the Fire Information for Resource Management System (FIRMS) has been used. The data was obtained from https://firms.modaps.eosdis.nasa.gov/map/.

4. Results

4.1 Case study 1: the Netherlands

Figure 4.1 presents the true color composite (Suomi NPP/VIIRS) image of the Netherlands from 19-04-2019 until 22-04-2019. The clouds present during the 22nd are clearly visible. The fire count data from FIRMS is shown in figure 4.2. The AOT and trace gases data over the Netherlands are presented in figure 4.3. The pixel size is not constant for each orbit and day. This is the result of the difference in pixel size below the nadir and more towards the end of the swath width. The effect of the wind, blowing from East direction towards West (table 4.1), is noticeable. Similarities in the spatial patterns of the different trace gases and AOT are not noticed from this data collection.

The clouds occurring at April 22nd seem to correspond with the pixels classified as Not Produced, Low AOT Quality and even Medium AOT Quality (see figure 4.5). The cloud pattern visible in the true color image, figure 4.1, is recognizable in figure 4.6 in the collection of pixels classified as being contaminated by the presence of clouds. The pattern is not clearly visible from the other products, with the exception of O_3. Pixels near the Waddenzee and the coastline seem to be repeatedly classified as Not Produced, Low AOT Quality and/or as cloudy.

Figure 4.4 presents the mapping of the AOT, CO and NO_2 data for a larger region covering the Netherlands, Belgium and Germany. The fire count data from FIRMS is plotted on top. Correspondence between the fire data and increased concentration of the pollutants can be seen. In the larger area, the transportation of the pollutants is more visible.

Figure 4.1: True color composite images (Suomi NPP/VIIRS) of the Netherlands from 19-04-2019 until 22-04-2019. Images obtained from https://worldview.earthdata.nasa.gov.

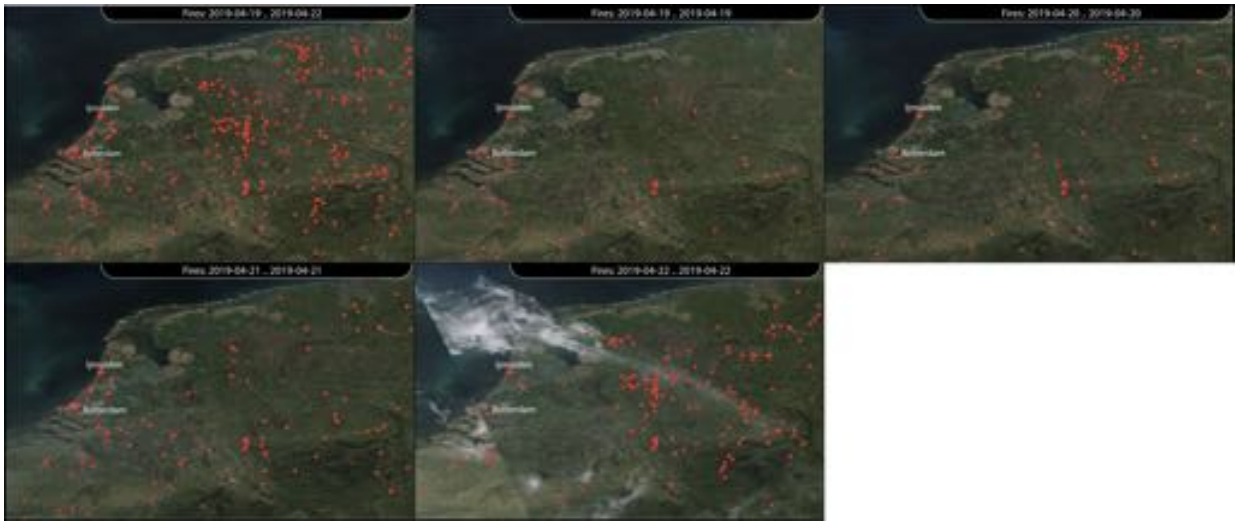

Figure 4.2: Satellite images (VIIRS) with in red the measured fires by VIIRS. Images obtained from FIRMS (Fire Information for Resource Management System) https://firms.modaps.eosdis.nasa.gov/map/. Note that some of the measured fires are not related to the Easter bonfires (e.g. near Industrial area's Ijmuiden and Rotterdam).

Day	Average wind speed [m/s]	Predominant wind direction
19-04-2019	3.5	76° (O)
20-04-2019	3.3	58° (ONO)
21-04-2019	2.1	60° (ONO)
22-04-2019	4.5	96° (O)

Table 4.1: Average wind speed and predominant wind direction measured in de Bilt (Lat: 52.10, Lon: 5.17), the Netherlands, at 19th-22nd of April 2019. Data obtained from: https://projects.knmi.nl/klimatologie/daggegevens/.

4.2 Case study 2: New Delhi

Figure 4.7 presents the true color composite image of the New Delhi region from the 30th of May until the 2nd of June 2019. An increasing haze is visible. Increasing pollutant values are to a certain extent visible in the AOT data (figures 4.8 and 4.9). Figure 4.8 presents a collection of mapped AOT data with varying QF masking settings. The amount of visible pixels decreased significantly after masking the medium AOT quality and the out of spec range AOT QF's. Part of the pixels classified as out of range seem to correspond with the cloud pattern visible in the true color images. It is difficult to see pollution transportation patterns in the residual pixels. Flow patterns are the most pronounced in the NO_2 and CO data (figure 4.9). Correspondence between the different pollution data cannot be recognized from the images.

Figures 4.10 and 4.11 show mapped QF's values of AOT Quality and AOT out of Spec Range respectively. In the mapped data of dates 30-05-2019, 31-05-2019 and 01-06-2019 a pattern of decreasing AOT quality from the East towards the West can be seen. The same pattern is noticeable in 4.11.

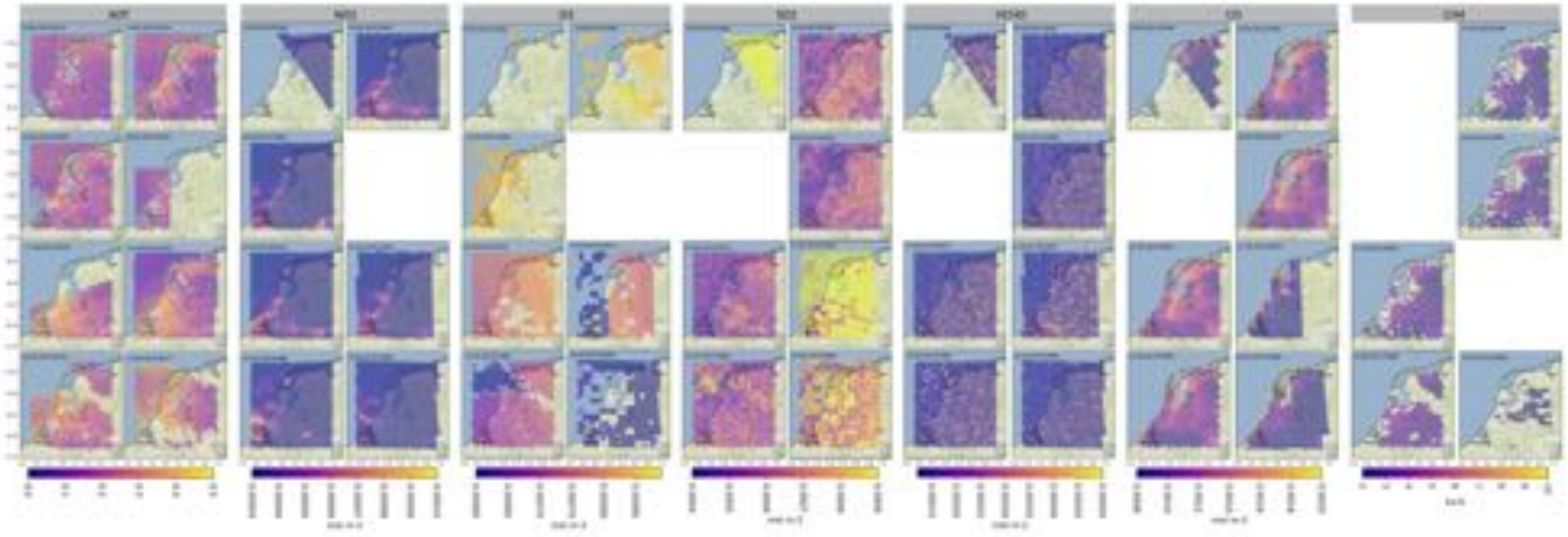

Figure 4.3: Mapped AOT, NO_2, O_3, SO_2, HCHO, CO and CH_4 data for 19, 20, 21 and 22nd of April 2019. Note that the AOT data is masked, such that only the medium and high quality AOT data is visible. The mapped region has a latitude between 51.2 and 53.7 and longitude between 3.3 and 7.2.

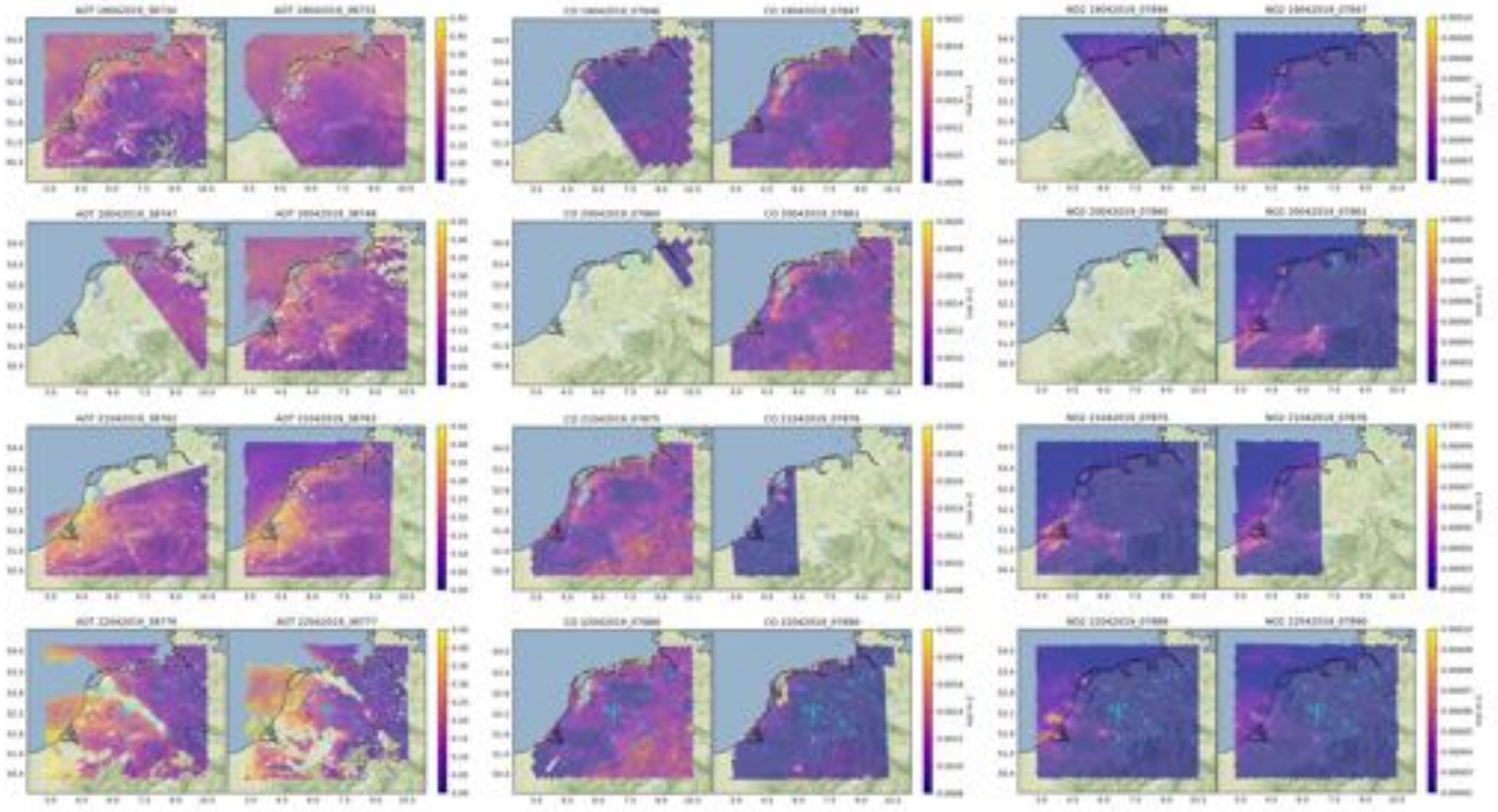

Figure 4.4: Mapped AOT, CO and NO_2 data for 19, 20, 21 and 22nd of April 2019. The AOT data is masked, such that only the medium and high quality AOT data is visible. The mapped region is expanded in order to follow the spatial transportation of the pollutions. The blue dots represent the measured fires by FIRMS (VIIRS data). The data is downloaded from `https://nrt3.modaps.eosdis.nasa.gov/archive/FIRMS/viirs/`. The mapped region has a latitude between50.2 and 54.2 and longitude between 2.7 and 10.6.

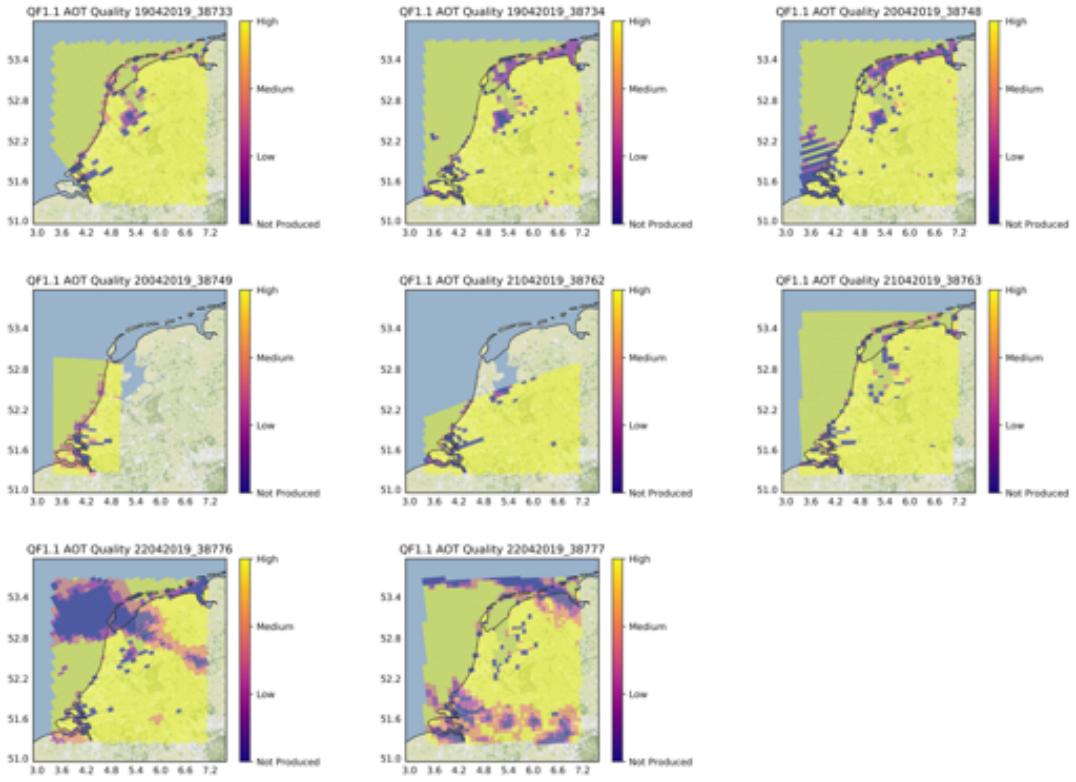

Figure 4.5: Mapped Quality Flag AOT values scenario 1.

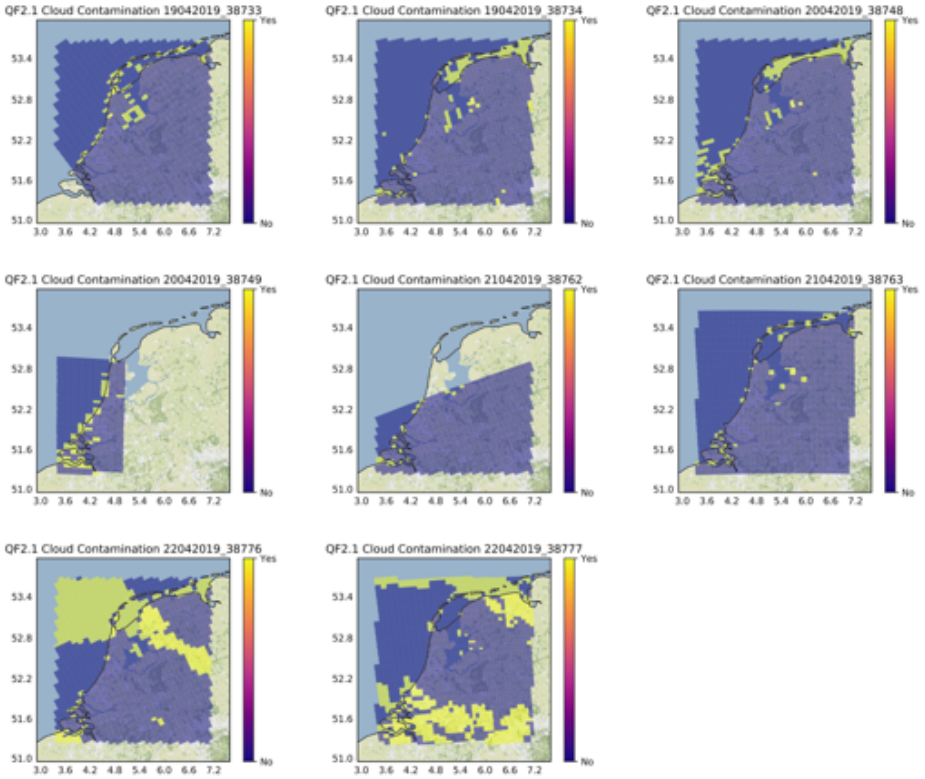

Figure 4.6: Mapped Quality Flag Cloud Contamination values scenario 1.

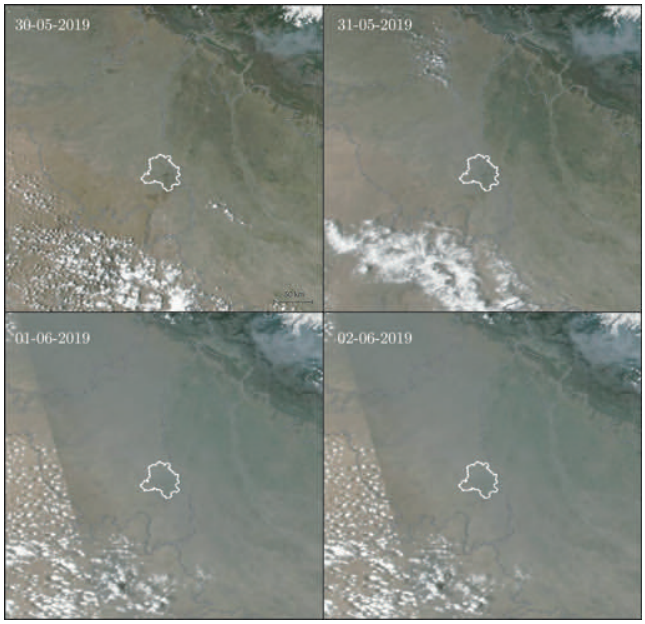

Figure 4.7: True color composite images (Suomi NPP/VIIRS) of the great New Delhi region from 30-05-2019 until 02-06-2019. Images obtained from `https://worldview.earthdata.nasa.gov`.

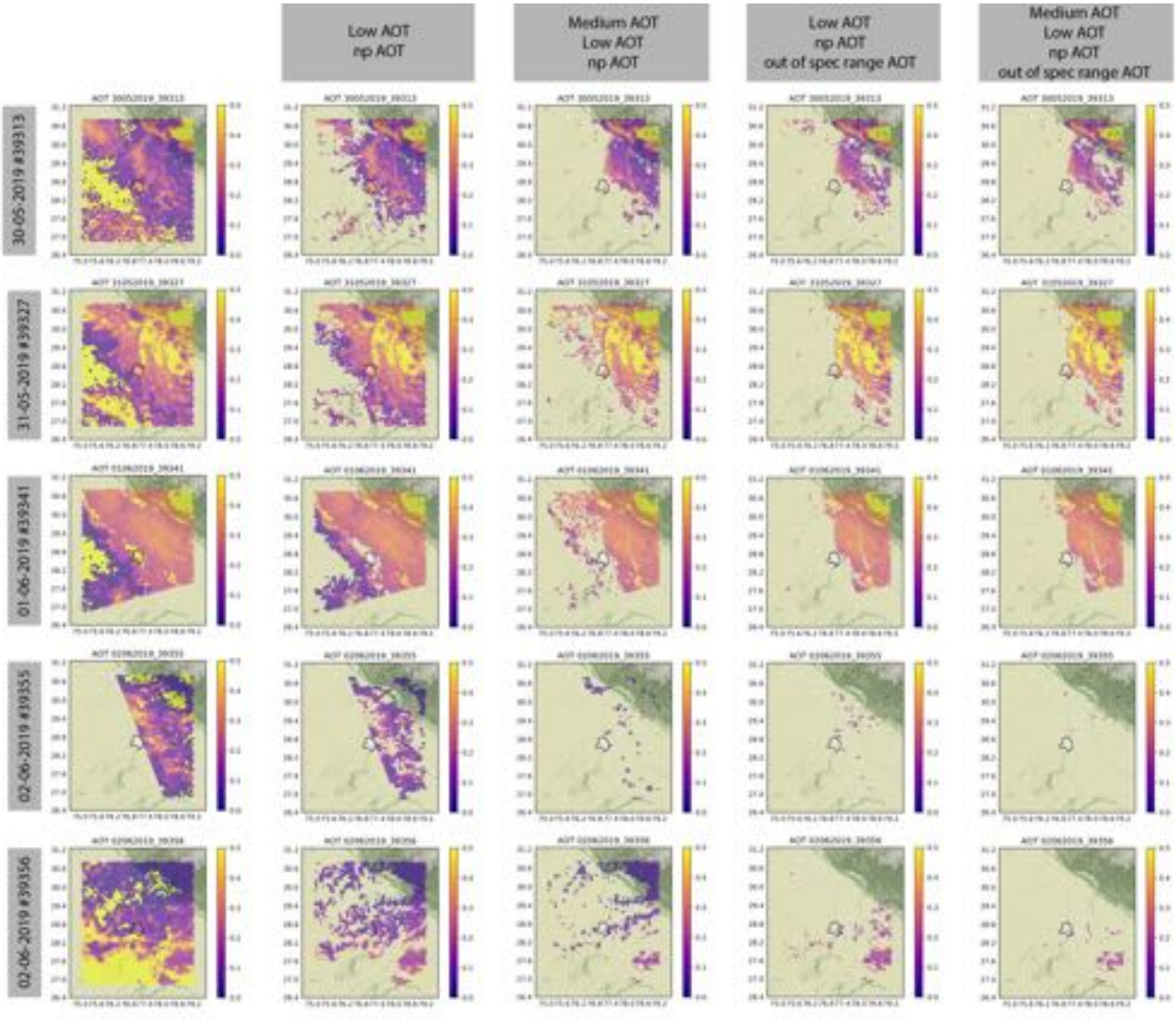

Figure 4.8: VIIRS EDR AOT data in the great New Delhi region (30-05-2019 until 02-06-2019). Various maps are presented, each with different QF masking settings. From left to right: i) all AOT data visible, ii) not produced and low AOT quality data masked, iii) not produced, low and medium AOT data masked, iiii) not produced, low AOT quality and out of spec range AOT data masked and iiiii) not produced, low and medium AOT quality and out of spec range AOT data masked.

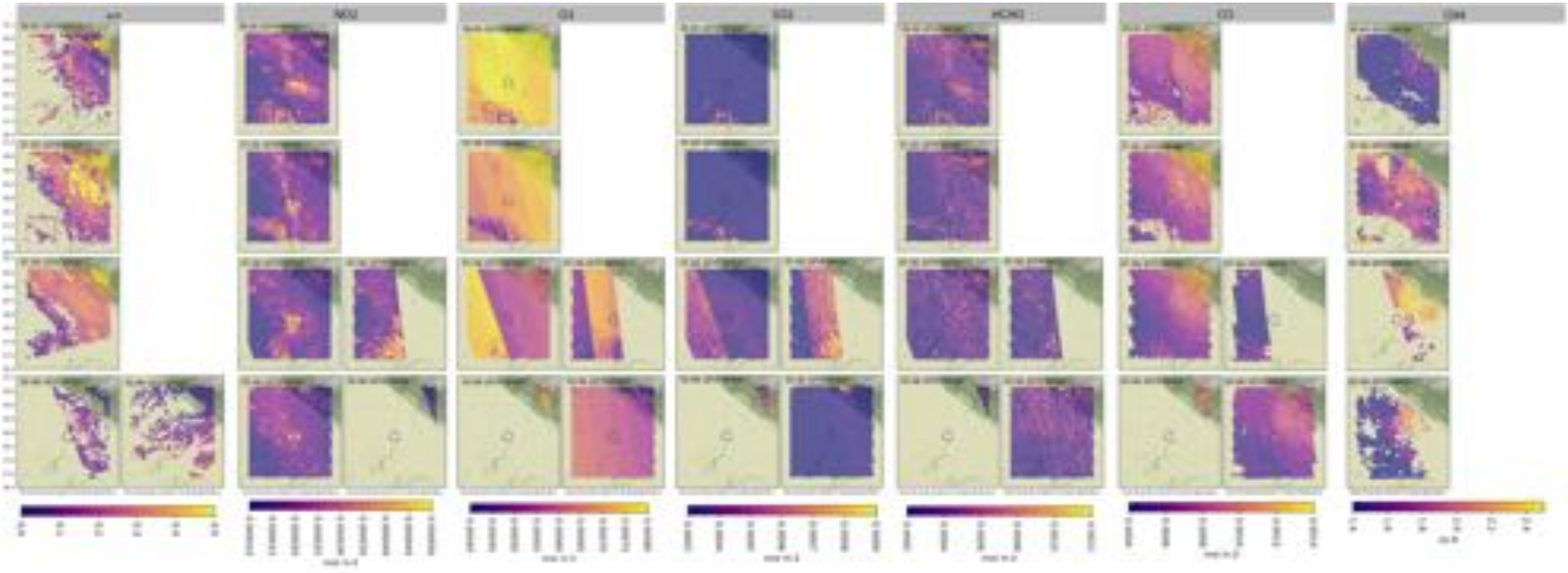

Figure 4.9: Mapped AOT, NO_2, O_3, SO_2, HCHO, CO and CH_4 data for 30-05-2019, 31-05-2019, 01-06-2019 and 02-06-2019. Note that the AOT data is masked, such that only the medium and high quality AOT data is visible. The mapped region has a latitude between 26.8 and 30.85 and longitude between 75.03 and 79.24.

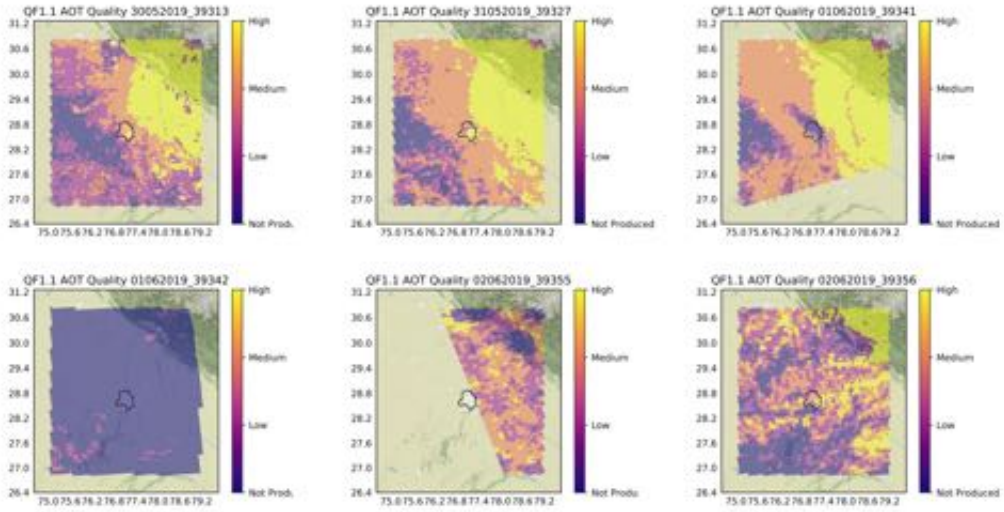

Figure 4.10: Mapped Quality Flag AOT Quality values scenario 2.

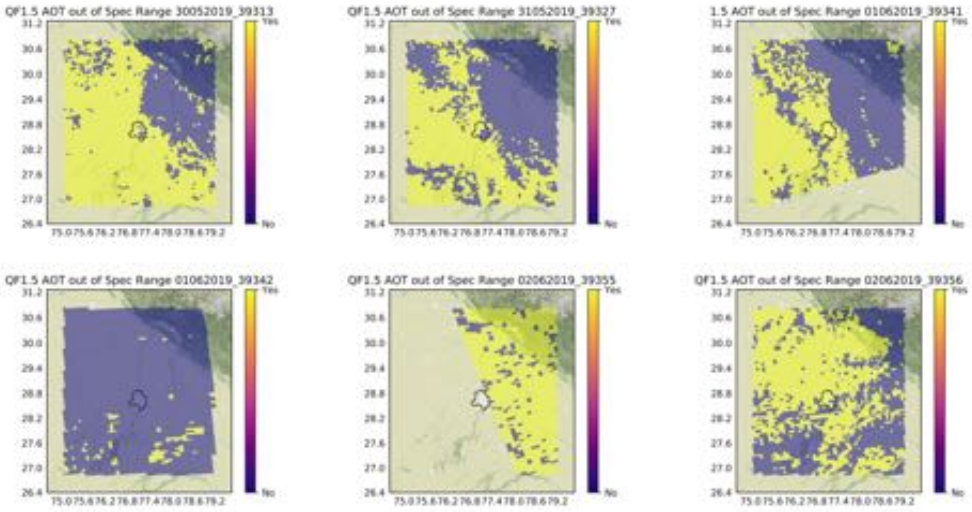

Figure 4.11: Mapped Quality Flag AOT out of Spec Range values scenario 2.

5. Summary, Conclusions and Recommendations

This project focussed on providing accessible tools for downloading and visualization of TROPOMI and VIIRS AOT data. Additional notice was taken on gaining insight on the VIIRS EDR Quality Flags. During this project, more understanding of VIIRS AOT and TROPOMI products and their data format has been developed. A main script, which makes use of additional scripts containing several functions, has been written that enables downloading and collection of the data by storing it in accessible and structured dictionary's. Furthermore, a VIIRS EDR QF analyzation and post-processing tool in the form of a GUI has been developed. The tool visualizes the data and allows masking QF values. Desired settings for the masking of QF values can be saved under a chosen name and stored inside a dictionary. The stored settings can be used to mask the specific values in a data set. For mapping of the data, of both TROPOMI trace gases and VIIRS EDR AOT, functions were written. In conclusion, scripts and tools have been developed which enables automatic downloading and visualization of multiple products for multiple days.

With the help of the developed tools, the air quality products from VIIRS and TROPOMI were mapped for two case studies: i) The first case study focussed on air pollution in the Netherlands as a result of traditional Easter fires. Transportation of the pollution was clearly visible in the East direction, corresponding with the predominant wind direction, for the AOT and NO_2 data. Furthermore, the higher pollution concentrations did coincide with the fire count data from FIRMS. The cloudy pattern appearing on the 22nd of April was visible in the QF Cloud Contamination and QF AOT Quality values. The correspondence of both QF's is not surprising, since QF AOT Quality uses data of pixel classifications, such as cloudiness, to determine the quality. However, the QF's Cloud Contamination and AOT Quality classified a significant amount of pixels near the coastline and the Waddenzee as cloudy and Not Produced or Low Quality. Most of these cloudy area's are not noticeable as cloud contamination in the true color map. ii) In the second case study air pollution products for a four-day series of the New Delhi region was mapped. This specific situation was interesting due to the increasing haze over time visible in the true color images. The number of suited pixels dropped significantly for more strict QF settings. An East to West decrease of the QF AOT quality and increase of the amount of AOT out of Spec Range pixels was noticeable. More research on this specific study will be needed in order to be able to draw conclusions regarding this striking pattern. A transportation process with changing wind direction is visible in the NO_2 map. Furthermore, transportation process can also be noticed in the CO data. The maps for the other trace gases are less clear and will need more studying. Therefore, for both case studies similarities in spatial patterns between the different trace gases and AOT data are difficult to detect.

In order to gain more understanding in the appeared repeating patterns of the QF values, statistical analyses will be needed. A gridding technique applied on a large dataset could be employed. Studying the statistics of QF values could potentially tell us more about the relation between the value and a specific geographic location. In addition, more understanding of the retrieval and of the used products themselves will be needed in order to draw conclusions. Recommendations regarding the developed tools are broadly discussed in the user manual.

References

Balis, D., Kroon, M., Koukouli, M., Brinksma, E., Labow, G., Veefkind, J., and McPeters, R. (2007). Validation of ozone monitoring instrument total ozone column measurements using brewer and dobson spectrophotometer ground-based observations. *Journal of Geophysical Research: Atmospheres*.

Bovensmann, H., Burrows, J., Buchwitz, M., Frerick, J., Noël, S., Rozanov, V., Chance, K., and Goede, A. (1999). Sciamachy: Mission objectives and measurement modes. *Journal of the Atmospheric Sciences*, 56(2):127–150.

Burrows, J. P., Platt, U., and Borrell, P. (2011). *The remote sensing of tropospheric composition from space*. Springer Science & Business Media.

Burrows, J. P., Weber, M., Buchwitz, M., Rozanov, V., Ladstätter-Weißenmayer, A., Richter, A., DeBeek, R., Hoogen, R., Bramstedt, K., Eichmann, K.-U., et al. (1999). The global ozone monitoring experiment (gome): Mission concept and first scientific results.

Dickinson, R. E. and Cicerone, R. J. (1986). Future global warming from atmospheric trace gases. *nature*, 319(6049).

Engel-Cox, J. A., Hoff, R. M., and Haymet, A. (2004). Recommendations on the use of satellite remote-sensing data for urban air quality. *Journal of the Air & Waste Management Association*, 54(11).

ESA (2019). Sentinel-5p satellite description - orbit. `https://sentinels.copernicus.eu/web/sentinel/missions/sentinel-5p/orbit`.

Gopalaswami, P. (2016). A study on effects of weather, vehicular traffic and other sources of particulate air pollution on the city of delhi for the year 2015. *Journal of Environment Pollution and Human Health*.

Graveland, H., Van Roosbroeck, S. A., Rensen, W. M., Brunekreef, B., and Gehring, U. (2011). Air pollution and exhaled nitric oxide in dutch schoolchildren. *Occupational and environmental medicine*, 68(8):551–556.

Gupta, P., Christopher, S. A., Wang, J., Gehrig, R., Lee, Y., and Kumar, N. (2006). Satellite remote sensing of particulate matter and air quality assessment over global cities. *Atmospheric Environment*, 40(30):5880–5892.

Jackson, J. M., Liu, H., Laszlo, I., Kondragunta, S., Remer, L. A., Huang, J., and Huang, H.-C. (2013). Suomi-npp viirs aerosol algorithms and data products.

Lambert, J., Keppens, D., Hubert, B., Langerock, Eichmann, K., Kleipool, Q., Sneep, M., Verhoelst, T., Wagner, T., Weber, M., Ahn, C., Argyrouli, A., Balis, D., Chan, K., Compernolle, S., De Smedt, I., Eskes, H., Garane, K., Gleason, J., Goutail, F., Granville, J., Hedelt, P., Heue, K., Jaross, G., Koukouli, M., Kumar Sha, M., Landgraf, J., Lutz, R., Niemejer, A., Pazmiño, A., Pommereau, J., Richter, A., Rozemeijer, N., Stein Zweers, D., Theys, N., Tilstra, G., Torres, O., Valks, P., and Wang, P. (2018). Quarterly validation report of the sentinel-5 precursor operational data products 01: July – october 2018.

Levelt, P. F., Joiner, J., Tamminen, J., Veefkind, J. P., Bhartia, P. K., Stein Zweers, D. C., Duncan, B. N., Streets, D. G., Eskes, H., McLinden, C., et al. (2018). The ozone monitoring instrument: overview of 14 years in space. *Atmospheric Chemistry and Physics*, 18(8):5699–5745.

Levelt, P. F. and Noordhoek, R. (2002). Omi algorithm theoretical basis document volume i. *ATBD. OMI-Ol, Version*, 1(1).

Martin, R. V. (2008). Satellite remote sensing of surface air quality.

Murphy, R. E., Barnes, W. L., Lyapustin, A. I., Privette, J., Welsch, C., DeLuccia, F., Swenson, H., Schueler, C. F., Ardanuy, P. E., and Kealy, P. S. (2001). Using viirs to provide data continuity with modis. In *IGARSS 2001. Scanning the Present and Resolving the Future. Proceedings. IEEE 2001 International Geoscience and Remote Sensing Symposium (Cat. No. 01CH37217)*, volume 3, pages 1212–1214. IEEE.

NASA (2019). Joint polar satellite system (jpss) viirs aerosol optical thickness (aot) and particle size parameter algorithm theoretical basis document (atbd).

NOAA NESDIS STAR (2013a). Suomi national polar-orbiting partnership (snpp) visible infrared imaging radiometer suite (viirs) aerosol products user's guide.

NOAA NESDIS STAR (2013b). Visible infrared imaging radiometer suite (viirs) sensor data record (sdr) user's guide.

NOAA NESDIS STAR (2014). Suomi national polar-orbiting partnership (snpp) visible infrared imaging radiometer suite (viirs) aerosol products user's guide.

Platt, U. and Stutz, J. (2008). *Differential Optical Absorption Spectroscopy*. Springer Science & Business Media.

Sanders, A. F., De Haan, J. F., and Veefkind, J. P. (2012). Retrieval of aerosol height from the oxygen a band with tropomi.

Seaman, C. (2013). Beginner's guide to viirs imagery data. Technical report, CIRA/Colorado State University.

Siddans, R. and Smith, A. (2018). Sentinel-5 precursor/tropomi level 2 product user manual npp cloud.

Slusser, J., Hammond, K., Kylling, A., Stamnes, K., Perliski, L., Dahlback, A., Anderson, D., and DeMajistre, R. (1996). Comparison of air mass computations. *Journal of Geophysical Research: Atmospheres*, 101(D5):9315–9321.

Theys, N., Hedelt, P., De Smedt, I., Lerot, C., Yu, H., Vlietinck, J., Pedergnana, M., Arellano, S., Galle, B., Fernandez, D., et al. (2019). Global monitoring of volcanic so 2 degassing with unprecedented resolution from tropomi onboard sentinel-5 precursor. *Scientific reports*, 9(1):2643.

van Geffen, J., Eskes, H., Boersma, K., Maasakkers, J., and Veefkind, J. (2019). Tropomi atbd of the total and tropospheric no2 data products.

Veefkind, J. (1999). *Aerosol satellite remote sensing*. PhD thesis, Universiteit Utrecht.

Veefkind, J. P., Aben, I., McMullan, K., Förster, H., De Vries, J., Otter, G., Claas, J., Eskes, H., De Haan, J., Kleipool, Q., et al. (2012). Tropomi on the esa sentinel-5 precursor: A gmes mission for global observations of the atmospheric composition for climate, air quality and ozone layer applications. *Remote Sensing of Environment*.

Voors, R., de Vries, J., Bhatti, I. S., Lobb, D., Wood, T., van der Valk, N., Aben, I., and Veefkind, P. (2012). Tropomi, the sentinel 5 precursor instrument for air quality and climate observations: status of the current design. In *International Conference on Space Optics—ICSO 2012*, volume 10564, page 105641Q. International Society for Optics and Photonics.

World Health Organization (2016). Ambient air pollution: A global assessment of exposure and burden of disease.